Investigation of selective oxidation during cooling of hot-rolled iron-manganese-silicon alloys

Xue Zhang [a,b], Cauê Corrêa da Silva [a], Siyuan Zhang [a], Manoj Prabhakar [a], Wenjun Lu [a], Alexandra Vogel [a], Michael Rohwerder [a,*]

[a] Max-Planck-Institut für Eisenforschung GmbH, Max-Planck-Straße 1, Düsseldorf, 40237, Germany
[b] Corrosion Center, Institute of Metal Research, Chinese Academy of Sciences, Shenyang, 110016, China

ABSTRACT

The kinetics of selective oxidation in iron-manganese-silicon alloys of varying silicon contents was examined at 700°C and oxygen partial pressure of 2.9×10^{-22} bar for up to 2 h. The investigation revealed a linear mass gain over time, suggesting oxygen uptake as the rate-controlling step of reaction. Internal oxidation depth particularly along grain boundaries increased considerably with increasing silicon content. Differences in microstructure and near-surface chemistry of the alloys as a function of the silicon content are discoursed on. The results point to the crucial role of a thin oxide layer, a solid solution between FeO and MnO, in the oxidation process.

1. Introduction

Advanced high strength steels, e.g., transformation-induced plasticity (TRIP) steel, are widely used in automotive body-in-white construction because of their high strength-to-density ratio and good ductility [1]. This allows a considerable reduction of sheet thickness and consequently the weight of auto-bodies becomes lighter, which helps to reduce CO_2 emissions and meet the demand for energy conservation. Hot-rolling of high strength steels is a primary step for making chassis and underbody components of automobiles. Manganese, silicon, aluminum and/or chromium are regarded as major alloying elements in high strength steels. However, oxide formation of these alloying elements underneath the external iron oxide scale formed after hot rolling impairs the mechanical properties of steels. Particularly when formed along grain boundaries (GBs), these oxides impair the cohesion between adjacent grains and can result in serious surface defects in post-processing such as pickling [2,3]. Therefore, understanding the internal oxidation process particularly along GBs is essential to develop novel protection strategies against high temperature oxidation.

Besides many works on the external scaling and descaling of steel sheets during hot rolling processes [4–7], the internal oxidation process has not been extensively studied. Kizu et al. [8] studied the intergranular and internal oxidation of an ultra-low carbon steel with 0.01 mass% Si after exposure to a mixed gas atmosphere (oxygen content of 1−10 vol.

%) at 1423−1563 K. Nevertheless, a deep understanding of the internal oxidation process is impeded due to the presence of thick oxide scales under those conditions. To suppress the growth of external iron oxide scales, the oxygen partial pressure needs to be reduced to below the Fe/FeO equilibrium partial pressures of oxygen at the respective annealing temperature, e.g. at 700 °C below 10^{-21} bar. For example, Auinger et al. [2] used a gas composition of $H_2/H_2O/Ar$ ($p(O_2) = 2 \times 10^{-22}$ bar) for a kinetic study on the internal oxidation of {Mn, Si, Al, Cr}-added iron-based alloys at 700 °C. For the selective oxidation process, the elemental diffusion was regarded as the rate controlling step. The authors also reported discrepancies between theoretical simulations and experiments. We previously investigated the selective oxidation of iron-manganese-silicon alloys exposed at $p(O_2) = 6.5 \times 10^{-25}$ bar at 700 °C and found that linear mass growth could last up to more than 1 or 2 h [9]. Under the very low oxygen partial pressure linear growth is expected at early stages, when oxygen uptake is the rate-determining step. It remains to be examined how such linear growth would proceed at higher oxygen partial pressures and during more extended timespans.

Selective oxidation at $p(O_2) = 6.5 \times 10^{-25}$ bar and 700 °C resembles the traditional conditions of recrystallisation annealing prior to hot dip galvanizing [10,11]. However, to avoid massive external oxidation, modern day annealing is conducted under much higher oxygen partial pressure. Therefore, in this study, we apply the condition $p(O_2) = 2.9 \times 10^{-22}$ bar at 700 °C to simulate a more realistic condition. The focus of
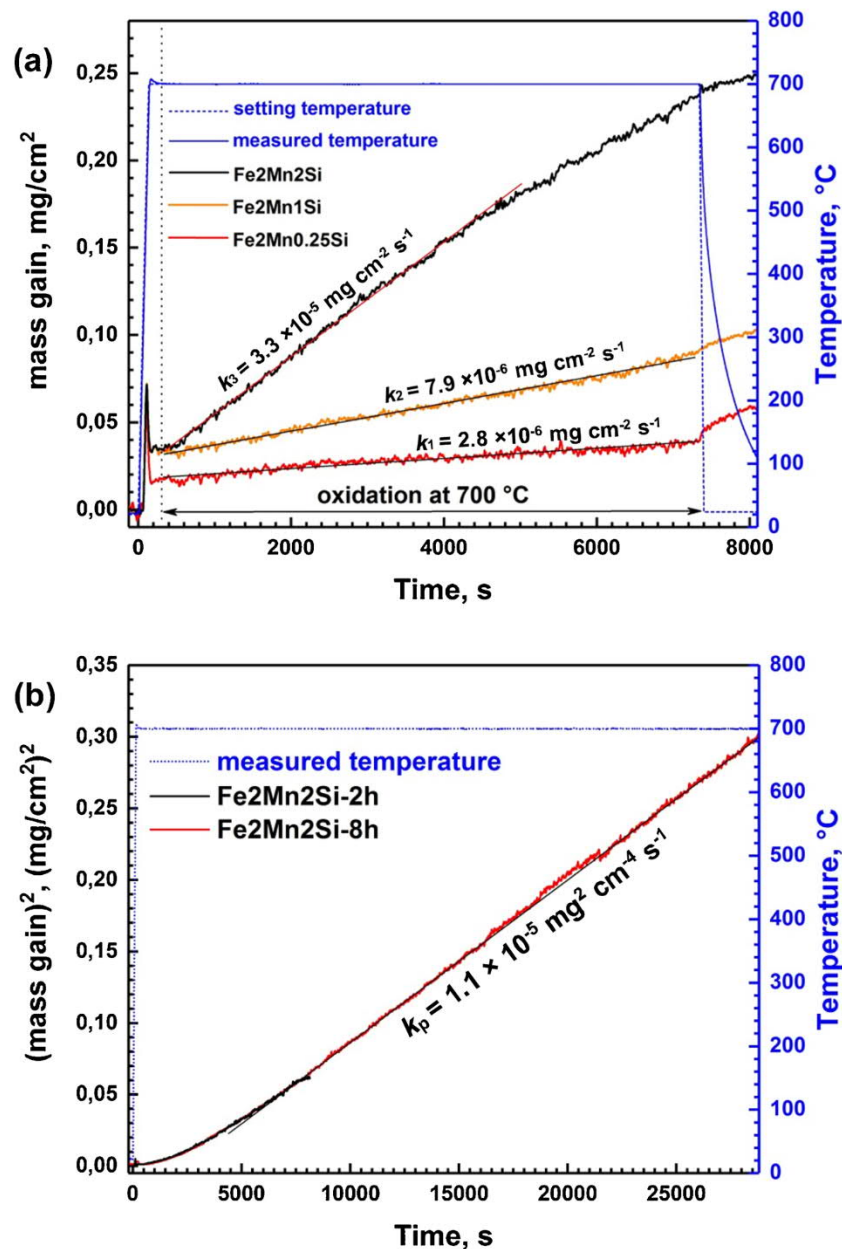
Fig. 1. Oxidation kinetics of iron-manganese-silicon of varying silicon concentrations during exposure at $p(O_2) = 2.9 \times 10^{-22}$ bar at 700 °C.

this work, however, is the external and internal oxidation resulting from much longer high temperature exposures, which is for instance relevant to internal oxidation during cooling after hot rolling. Especially the significant grain boundary oxidation which is observed for some higher alloyed steels is a considerable problem as it was found to cause severe selective grain boundary attack during pickling [2].

Hence, the partial pressure of oxygen in this research was chosen as a value marginally lower than that thermodynamically required for wüstite formation. This experimental approach ensures conditions quite close to those underneath a dense wüstite scale, and thus should provide a good approach for studying the fundamentals of selective oxidation beneath the wüstite scale and of the role of alloy composition on the oxidation kinetics under these conditions. Among the most important alloying additions in steel manufacturing, the combination of Mn and Si results in internal oxidation up to higher depths and along grain boundaries. Therefore, Fe-Mn-Si alloys of varying Si contents were used as model alloys in this study. To obtain mass gain signals containing reliable information starting from the onset of oxidation, a highly

sensitive in-situ thermogravimetry, developed in-house, was employed. Since the wüstite scale formation is prevented by adjusting the oxygen partial pressure to a value below the equilibrium partial pressure of Fe/FeO, the mass gain directly provides information about the extent of selective oxidation. Surface and subsurface chemistry as well as microstructure of the alloys after exposure were examined by combining different analytical techniques. The main objectives of this research were to gain an insight into the oxidation kinetics of Fe-Mn-Si alloys at comparatively high oxidation partial pressure (close below the Fe/FeO equilibrium) and unravel the processes determining the often-surprising high depth of internal oxidation of Fe-Mn-Si especially along grain boundaries.

2. Material and methods

Low alloyed Fe-2 Mn-x Si alloys with a Mn content of 2 mass% and Si content of either 0, 0.25, 1 or 2 mass% were prepared in-house by casting, subsequently formed to sheets by hot rolling. The sheets were
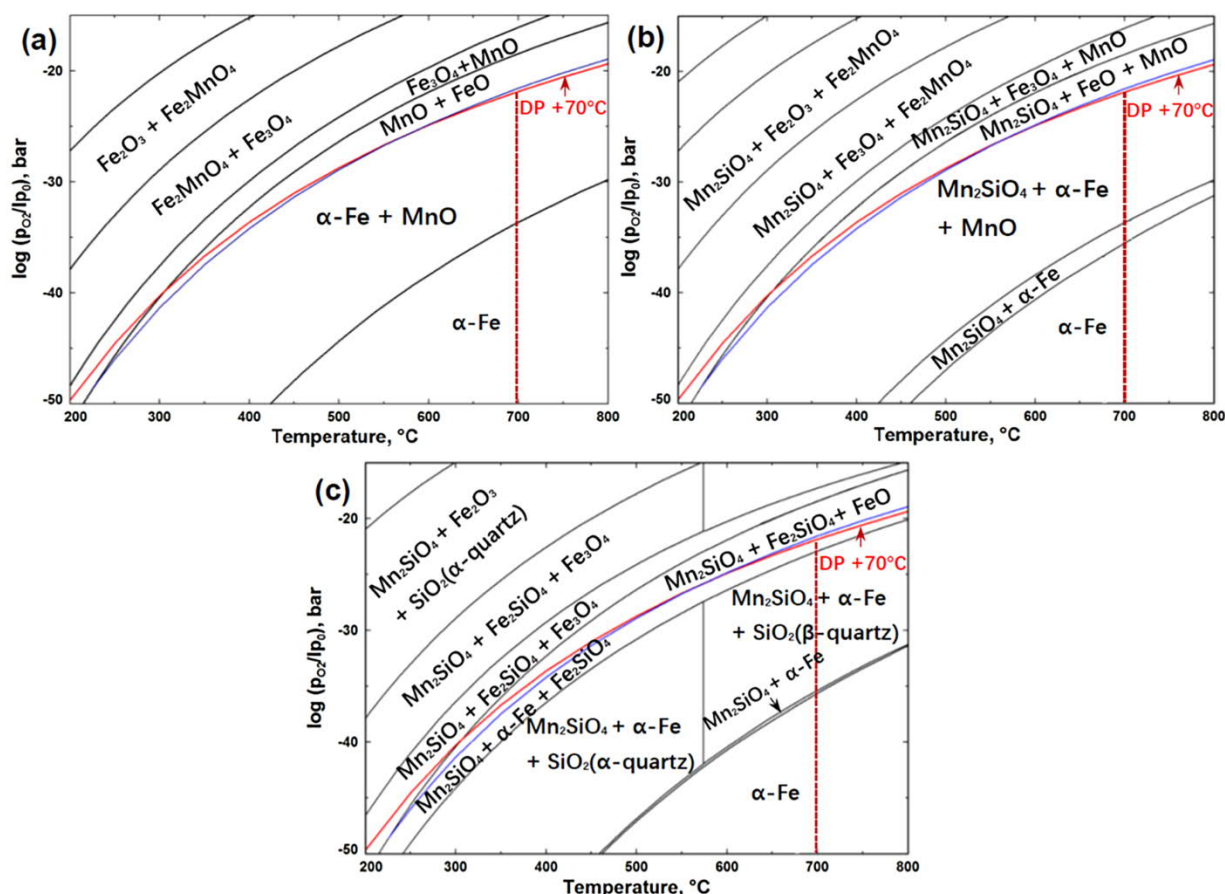
Fig. 2. Partial pressure of oxygen vs. temperature phase diagrams for Fe-2 Mn (a), Fe-2 Mn-0.25 Si (b) Fe-2 Mn-1 Si and Fe-2 Mn-2 Si (c). *Blue line* $p(O_2)$ of Fe/FeO equilibrium calculated by HSC Chemistry 6.0; *Red line* $p(O_2)$ in the H_2/H_2O gas (69 vol%/31 vol%, +70 °C dew point). (For interpretation of the references to colour in this figure legend, the reader is referred to the web version of this article).

cut to rectangular coupons with a size of $10 \times 10 \times 2$ (mm), ground and subsequently polished to a 1-μm finish. Selective oxidation studies were conducted in a self-developed thermogravimetric analysis equipment with ultra-high sensitivity. Details of the experimental set-up have been described in Ref. [12]. To shorten the heating time and hence eliminate the influence of oxidation during heating, an infra-red furnace was employed to heat the sample, with the temperature program set to a very fast heating ramp of 5 K s^{-1}. The gas atmosphere consisted of 69 vol% H$_2$ and 31 vol% H$_2$O, corresponding to +70 °C dew point at a total partial pressure of 1 bar (DP +70 °C), and the total pressure in the chamber was maintained at 40 mbar. The exclusive use of reactive gas species, i.e. without the usual carrier gas of nitrogen or argon, in a low-pressure environment is beneficial for an enhanced signal-to-noise ratio, attributed to notably reduced atmospheric turbulences particularly right after rapid heating. All process parameters like the measured temperature, mass change and pressure were recorded automatically every second, using an in-house developed software. The thermogravimetry measurements for each type of alloy were conducted thrice to ensure repeatability.

For thermodynamic description of the system, the FactSage software (SGPS database) was employed and the calculation of stable phases was carried out based on the alloy composition, temperature and oxygen partial pressure. It is understandable that the thermodynamic data in different databases may vary to some extent due to the limitations of the theoretical and experimental methods. The oxygen partial pressure for the Fe/FeO equilibrium calculated by FactSage ($p(O_2) = 1.4 \times 10^{-22}$ bar at 700 °C) is slightly lower than the conditions of interest here, i.e. $p(O_2) = 2.9 \times 10^{-22}$ bar at 700 °C, whereas that calculated by HSC Chemistry 6.0 software is slightly higher. Hence, pure Fe was exposed at the

atmosphere of H$_2$/H$_2$O (69 vol%/31 vol%) at 700 °C to check whether it could be oxidized under such conditions. According to Fig. A1, no iron oxides can be observed after exposure for 2 h. This indicates that the partial pressure of oxygen in the 69 vol% H$_2$ + 31 vol% H$_2$O gas atmosphere is below the equilibrium between iron and wüstite and hence is suitable to resemble the oxygen activity underneath the external wüstite scale.

Phase analysis of the iron-manganese-silicon alloys after exposure was performed using grazing incidence X-ray diffraction (GIXRD) with generator voltage and tube current of 40 kV and 30 mA, respectively. Two samples for each type of alloy were measured by GIXRD to guarantee repeatability. Microscopic morphologies and elemental compositions of each type of alloy were measured using scanning electron microscopy equipped with an energy-dispersive X-ray detector (SEM/EDX). The cross sections of all the SEM samples were prepared by mounting the cut samples into resin, mechanically grinding down to 4000 grit and polishing with 50 nm SiO$_2$ suspension. The SEM/EDX measurements were carried out on at least two different samples for each type of alloy and on plentiful positions on each sample. Transmission electron microscope (TEM) as well as scanning transmission electron microscope (STEM) were employed to analyze the oxides at higher resolution. Cross-sectional TEM lamella was prepared by cutting from a typical region of an oxidized sample using a focused ion beam instrument (FIB, Scios2). A carbon marker layer was applied to protect the surface oxide layer from ion beam damage [13]. TEM experiments were performed on a JEOL 2200 microscope operated at 200 kV. STEM experiments were conducted at 300 kV on a Titan Themis microscope. High angle annular dark field (HAADF) STEM images were recorded using an integrated detector collecting diffracted angles between 73 and

200 mrad. STEM-EDX spectrum imaging was acquired using a four-quadrant SuperX spectrometer. The datasets were analyzed using multivariate statistical analysis to enhance the signal to noise level of the X-ray emission peaks [14]. Both the TEM and STEM investigations were carried out at least on three different positions of one sample to ensure repeatability. Further chemical analysis was performed using X-ray photoelectron spectroscope (XPS) with an Al K_α radiation source (1486.6 eV). The specimen surfaces were sputtered with argon ions (2.0 kV) for depth profiling. The sputtering rate was ~30 nm/min, calculated using calibration done on a SiO_2 sample and correlating it to the steel sample (this routine was found to be reasonable by comparing XPS depth profiles with SEM and TEM micrographs of cross sections). Peak fitting of the XPS peaks was performed in the CasaXPS software package. The XPS data were calibrated for charge shift by normalizing binding energies to that of the adventitious C 1s peak at 284.6 eV.

3. Results and discussion

3.1. Oxidation kinetics

The kinetics of oxidation of all analyzed ternary alloys during the selective oxidation heat treatment are presented in Fig. 1. A well-defined fast heating ramp (5 K s^{-1}) causes a slight overheating in the beginning of the experiment, which is then quickly stabilized at the desired isothermal temperature of 700 °C after ~160 s of annealing. After a short (and unavoidable) disturbance caused by the buoyancy effect, data with a pronounced signal-to-noise ratio can be precisely recorded. Alloys with higher Si content exhibit faster oxidation kinetics, as displayed in Fig. 1a. The mass gain of the Fe-2 Mn alloy is below the resolution limit of the thermogravimetry set-up (less than 10 μg cm^{-2}), and is hence not shown. The reaction kinetics of Fe-2 Mn-0.25 Si and Fe-2 Mn-1 Si follow a linear weight increase during 2 h of heat treatment, with linear rate constant values of 2.8×10^{-6} (k_1) and 7.9×10^{-6} (k_2) mg cm^{-2} s^{-1}, respectively. For ~4500 s, the mass of Fe-2 Mn-2 Si also increased linearly at a rate $k_3 = 3.3 \times 10^{-5}$ mg cm^{-2} s^{-1}, before entering a parabolic regime. The linear mass gain of the Fe-2 Mn-x Si alloys indicates that the probable rate-limiting step at early oxidation stage is the oxygen uptake (discussed in Section 3.4 in detail). Considering the much higher oxygen partial pressure in the study (compared to [9]), it is surprising to observe the early oxidation stage (rate controlled by oxygen uptake) lasting over 1~2 h.

In order to confirm the parabolic behavior of Fe-2 Mn-2 Si after the initial oxidation stage, the alloy underwent an extended heat treatment of 8 h. The resulting mass gain squared per unit area, Δw^2, is plotted over time, t (Fig. 1b). A visibly growing slope illustrates that the linear mass gain in the beginning of the selective oxidation annealing transitions to parabolic ($k = 1.1 \times 10^{-5}$ mg^2 cm^{-4} s^{-1}) mass gain after ~1.7 h of annealing. As the growing network of internal oxides eventually hinders elemental diffusion, the latter would become the rate-determining step of oxidation, characterized by the parabolic growth. Together with the results shown in Fig. 1a, it is clear that all the Fe-2 Mn-x Si alloys exhibit linear growth for relatively short-term oxidation and hence their initial oxidation process is determined by oxygen uptake rather than diffusion. It should be emphasized that the thermogravimetry results in this study are highly reproducible, as depicted by the total coincidence of both curves in Fig. 1b.

3.2. Morphology and structure of the oxides

Fig. 2 depicts the phase diagrams (oxygen partial pressure vs. temperature) of Fe-2 Mn-x Si alloys of varying Si contents. The partial pressure of oxygen in the prevailing 69 vol%H_2 + 31 vol%H_2O gas atmosphere is slightly lower than the critical value thermodynamically required for the FeO formation at 700 °C, but is high enough to oxidize Si and Mn in the whole temperature range. Under the existing temperature and partial pressure conditions, the stable thermodynamic phases
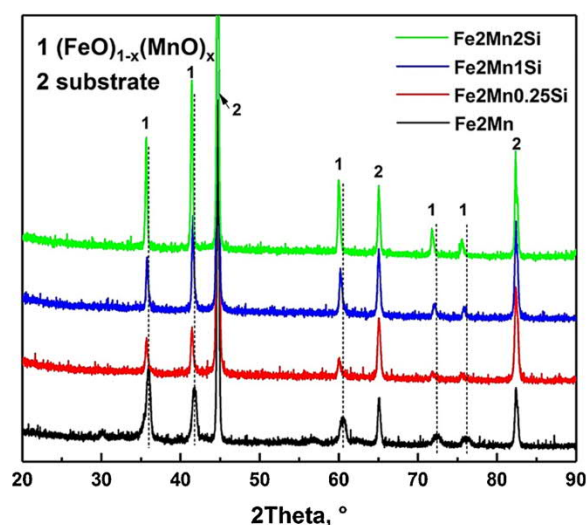

Fig. 3. GIXRD patterns of iron-manganese-silicon alloys of varying silicon concentrations post oxidizing at 700 °C and $p(O_2) = 2.9 \times 10^{-22}$ bar for 2 h.

are α-Fe + MnO for Fe-2 Mn, α-Fe + Mn_2SiO_4 + MnO for Fe-2 Mn-0.25Si and α-Fe + Mn_2SiO_4 + Fe_2SiO_4 for Fe-2 Mn-1 Si and Fe-2 Mn-2 Si.

GIXRD patterns of Fe-2 Mn, Fe-2 Mn-0.25 Si, Fe-2 Mn-1 Si and Fe-2 Mn-2 Si after exposed to aforementioned conditions for 2 h are shown in Fig. 3. The dominating peaks come from the $(FeO)_{1-x}(MnO)_x$ phase on the surface of the alloys [15]. The absence of $(FeO)_{1-x}(MnO)_x$ in the phase diagrams for all the Fe-2 Mn-x Si alloys shown in Fig. 2 is because of insufficient thermodynamic data in the database. Noticeably, adding Si into the alloys leads to a slight shift of the characteristic peaks of $(FeO)_{1-x}(MnO)_x$ towards lower angles, i.e., larger lattice parameters. This might occur because of a higher fraction of FeO in the $(FeO)_{1-x}(MnO)_x$ phase and/or the doping of Si into the $(FeO)_{1-x}(MnO)_x$ crystal and the corresponding lattice expansion. XRD did not detect any crystalline SiO_2 or Mn-Si oxide phases.

The surface morphologies of the Fe-2 Mn-x Si alloys after annealing are depicted in Fig. 4. The corresponding EDX results of the selected points are shown in Table 1. Some scattered $(FeO)_{1-x}(MnO)_x$ particles are formed on the Fe-2 Mn surface mainly along GBs. For Si-containing alloys, pronounced oxidation along grain boundaries develops as large ridges, which is also ascribed to $(FeO)_{1-x}(MnO)_x$. For Fe-2 Mn-2 Si, besides the preferential formation of oxides on the grain boundaries, a large number of $(FeO)_{1-x}(MnO)_x$ nodules are also widely distributed on the grains. The external $(FeO)_{1-x}(MnO)_x$ nodules are formed by outward diffusion of Fe and Mn to the surface and their subsequent oxidation. As the volume expansion by internal oxidation drives the outward diffusion, alloys with higher Si contents have higher degrees of internal oxidation and hence more external oxide nodules. The formation of the external nodules as a consequence of internal oxidation has also been reported previously [9,16–18].

According to the EDX results (Table 1), the Fe/Mn ratio in $(FeO)_{1-x}(MnO)_x$ increases with Si content, with values of approximately 0.8 (point 1), 1.8 (point 2), 3.4 (point 3) and 3.4 (point 4) for Fe-2 Mn, Fe-2 Mn-0.25 Si, Fe-2 Mn-1 Si and Fe-2 Mn-2 Si, respectively. To exclude the counts from the underlying metallic Fe matrix, the concentration of oxidized Fe is calculated by using the total O concentration subtracting the O concentration consumed for oxidizing Mn and Si (i.e., subtracting Mn and double of Si concentrations). The correlation between iron/manganese ratio of the oxides and silicon content of the alloy is in good agreement with the XRD results. Meanwhile, a slight amount of Si can be detected in the oxide nodules of Fe-2 Mn-1 Si and Fe-2 Mn-2 Si, as shown in Table 1, which might also be induced by the tensile stress formed during internal oxidation.

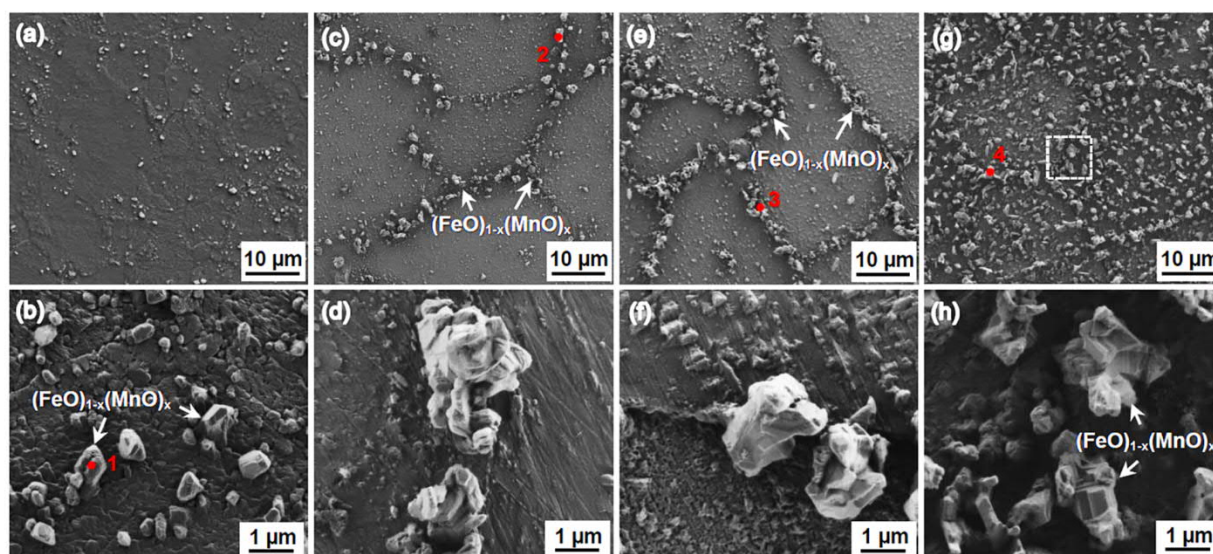Cross-sectional images of the Fe-2 Mn-x Si alloys of varying Si

Fig. 4. Surface morphologies of Fe-2 Mn (a, b), Fe-2 Mn-0.25Si (c, d), Fe-2 Mn-1Si (e, f) and Fe-2 Mn-2Si (g, h) post oxidizing at 700 °C and $p(O_2) = 2.9 \times 10^{-22}$ bar for 2 h.

Table 1
EDX analysis of the selected points in Fig. 4.

Element (at.%)	O	Fe	Mn	Si
Point 1	30.4	52.4	17.2	–
Point 2	36.5	50.4	13.1	–
Point 3	23.0	71.3	4.9	0.8
Point 4	19.1	76.2	4.1	0.6

contents after the aforementioned annealing conditions are shown in Fig. 5. For Fe-2 Mn, dispersed $(FeO)_{1-x}(MnO)_x$ oxides are precipitated both inside the grains and along the grain boundaries. The larger oxides are formed preferentially at the near-surface grain boundaries approximately 1 μm below the surface (Fig. 5b). Although the oxidation depth of Fe-2 Mn reaches a value of ~6.2 μm, only a small number of fine oxides are present at the oxidation front, mainly at grain boundaries, as shown in Fig. 5a. It is clear from Fig. 5b that the overall oxide size decreases progressively from the surface towards the oxidation front. Internal oxidation is accelerated significantly on adding Si to Fe-2 Mn. This results in a much higher oxide volume fraction and notably enhanced oxidation along the grain boundaries. These oxides are in average smaller than those without Si. Furthermore, the oxidation depth of Fe-2 Mn-x Si increases with silicon content, ~7.0, 9.9, and 14.6 μm for Fe-2 Mn-0.25 Si, Fe-2 Mn-1 Si, and Fe-2 Mn-2 Si, respectively. The size of some GB oxides in Fe-2 Mn-0.25Si is similar to that in Fe-2 Mn, and remarkedly larger than those in Fe-2 Mn-1 Si and Fe-2 Mn-2 Si. According to the phase diagram of Fe-2 Mn-0.25 Si (Fig. 2b), MnO coexists with Mn_2SiO_4 within a wide range of oxygen activity below the onset of the FeO formation. Therefore, these relatively large oxides in Fe-2 Mn-0.25 Si can be $(FeO)_{1-x}(MnO)_x$, whereas the smaller ones are Si-containing oxides. This is similar to our previous observation that relatively large MnO oxides were formed at the grain boundaries of Fe-2 Mn-0.25 Si after annealing at 700 °C and $p(O_2) = 6.5 \times 10^{-25}$ bar for 2 h [9].

For the alloys with higher Si contents, the grain boundary oxides are much smaller and finely dispersed. This is because nucleation of internal oxides is easier for alloys with higher Si contents. As the silicon content increases from 0.25 to 1 mass%, the depth of the grain boundary oxidation shows a limited increase, while intragranular oxidation develops principally. As the silicon content further raised to 2 mass%, both the density and the depth of the intragranular oxides increase remarkedly. The fronts of intragranular oxidation and GB oxidation almost coincide for alloys with higher contents of Si. Interestingly, the zoomed-in image of Fe-2 Mn-2 Si illustrates the existence of an external film-like oxide layer of ~100 nm thickness. It is worth noting that for all the alloys, the oxidation degree in different grains varies to some extent, as they have different crystallographic orientations.

Assuming oxygen diffusion as the rate-determining step for the internal oxidation of Fe-2 Mn-x Si, the extended Wagner's model (Meijering's model) [19] would result in calculated oxidation depths of 1.13, 0.91 and 0.75 μm for Fe-2 Mn-0.25 Si, Fe-2 Mn-1 Si and Fe-2 Mn-2 Si, respectively (taking diffusion coefficients of Mn, Si and O in α-Fe from Ref [20–22].). These calculated depths are apparently much lower than the experimental measurements. Therefore, oxygen diffusion coefficients in the studied alloys would be higher than the value in α-Fe. Since all the mass gain curves exhibit linear growth kinetics for the first 1~2 h, the diffusion must be even higher so that it is not rate limiting. The enhanced O diffusivity is probably attributed to the quite high density of oxides in the silicon-containing alloy matrix and a correspondingly reinforced mobility at the alloy/oxide interface [9,19].

The fine-scale external and internal microstructure of the oxides was further characterized by TEM. Fig. 6 displays the TEM micrographs of Fe-2 Mn after exposure to the 69 vol%H_2 + 31 vol%H_2O gas atmosphere for 2 h. A continuous oxide layer is identified on the surface of Fe-2 Mn. The external layer has a thickness ranging from several tens of nanometers to several hundreds of nanometers. Internal oxides were found dispersed inside the grains and at the grain boundaries. The selected area diff ;raction pattern of a big GB oxide (area A) located ~600 nm from the surface confirms that it has the wüstite phase $(FeO)_{1-x}(MnO)_x$ [15], which agrees with the XRD results. According to the EDX measurement in Fig. 6b, the external oxide layer has a much higher Fe content than the internal oxide. The Fe/Mn ratio in the external $(FeO)_{1-x}(MnO)_x$ is as high as 3.7 for point 1, but drops significantly for the internal oxide just ~200 nm below the surface (~0.8 for point 2). At increasing depth, the Fe/Mn ratio in $(FeO)_{1-x}(MnO)_x$ further decreases to ~0.6 for point 3. It is expected that only MnO is present at the front of internal oxidation, where the partial pressure of oxygen is too low to stabilize $(FeO)_{1-x}(MnO)_x$.

STEM observations of Fe-2 Mn-1 Si after heat treatment for 2 h at 700 °C and the corresponding elemental maps are displayed in Figs. 7 and 8. Fig. 7 depicts the external nodule-like oxides formed near the surface grain boundary are mainly composed of Fe, Mn and O, corresponding to $(FeO)_{1-x}(MnO)_x$ as defined previously. Fig. 8 shows the zoomed-in TEM images and elemental maps of the external film-like oxides and the
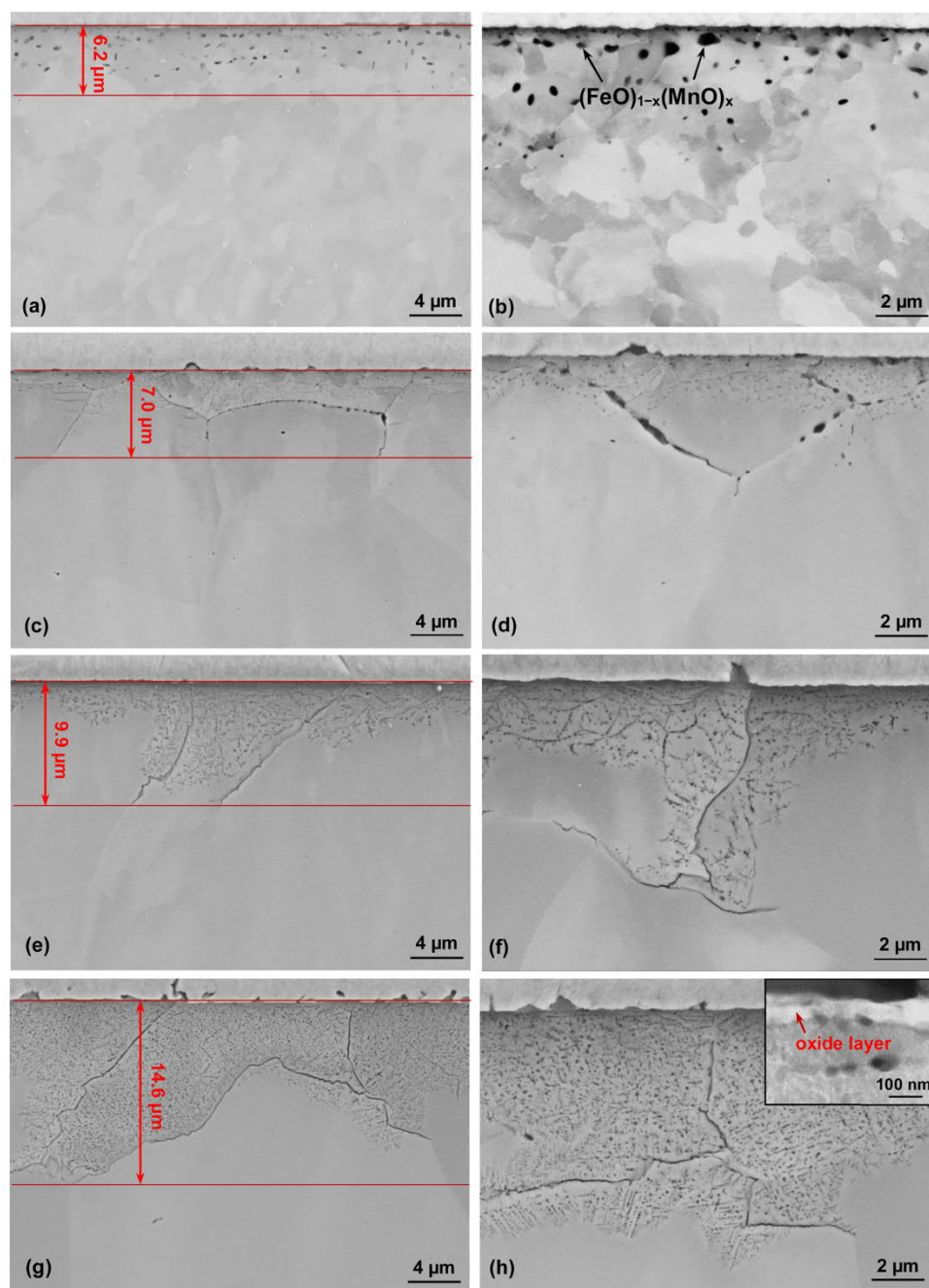
Fig. 5. Cross-sectional morphologies of Fe-2 Mn (a, b), Fe-2 Mn-0.25 Si (c, d), Fe-2 Mn-1 Si (e, f) and Fe-2 Mn-2 Si (g, h) post oxidizing at 700 °C and $p(O_2) = 2.9 \times 10^{-22}$ bar for 2 h.

internal oxides of Fe-2 Mn-1 Si. The oxide layer on the surface is composed primarily of $(FeO)_{1-x}(MnO)_x$ (doped with Mn-Si-mixed oxides), with a thickness of ~60 nm. Spherical Mn-Si oxides are finely dispersed close to the surface. The formation of the fine oxides near the surface is due to a higher oxygen activity in this region and correspondingly larger driving force for nucleation. The size of Mn-Si oxides increases with the distance from the surface, whereas their number density decreases (Fig. 8a). Further down to the oxidation front (3~5 μm from the surface), the internal oxides only consist of SiO_2, as illustrated in Fig. 8b. Around this region, oxides with a SiO_2 core and MnO shell are also found (Fig. 8b), in contrast to the homogeneous distribution of Mn and Si within the oxides close to the surface.

The variation in the oxide composition from the core to the shell can be attributed to the different $p(O_2)$ for the thermodynamic commencement of various oxides. The equilibrium oxygen pressure for Si/SiO_2 (2.9×10^{-39} bar at 700 °C) is significantly lower than those for Mn-rich oxide species (e.g., 4.5×10^{-33} bar of the equilibrium between Mn and MnO at 700 °C). This promotes formation of silica once the activity of O in the matrix has increased to the value of thermodynamic commencement for forming silica. Subsequently, Mn-rich oxides nucleate and grow on the silica nucleus. With time, the core-shell structure is supposed to be gradually transformed into a fully mixed Mn-Si oxide, as indicated by the already homogeneous oxides in the upper regions of the alloy.

3.3. Chemical analysis of the oxides

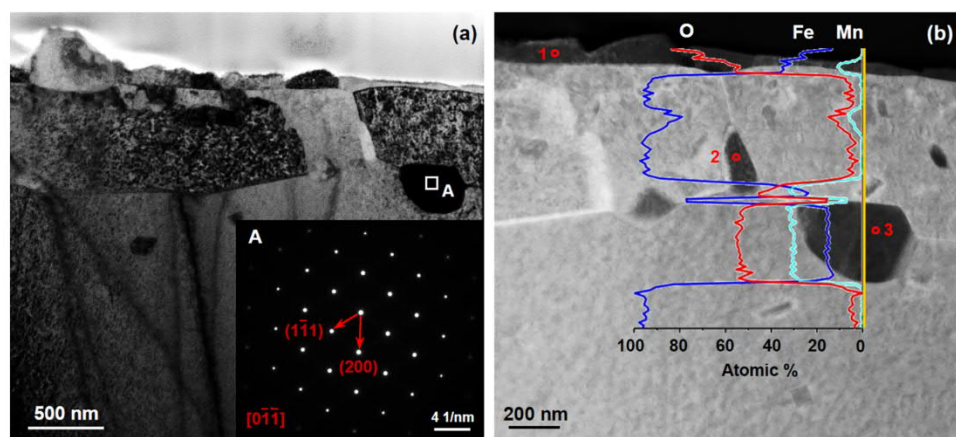The near-surface composition of alloys plays a crucial role in the

Fig. 6. TEM micrographs of Fe-2 Mn after exposure to the 69 vol%H_2 + 31 vol%H_2O gas atmosphere for 2 h at 700 °C (a, b) and the selected area diff ;raction pattern of the internal oxide (A) in (a) and the elemental line-scan measurement in (b).
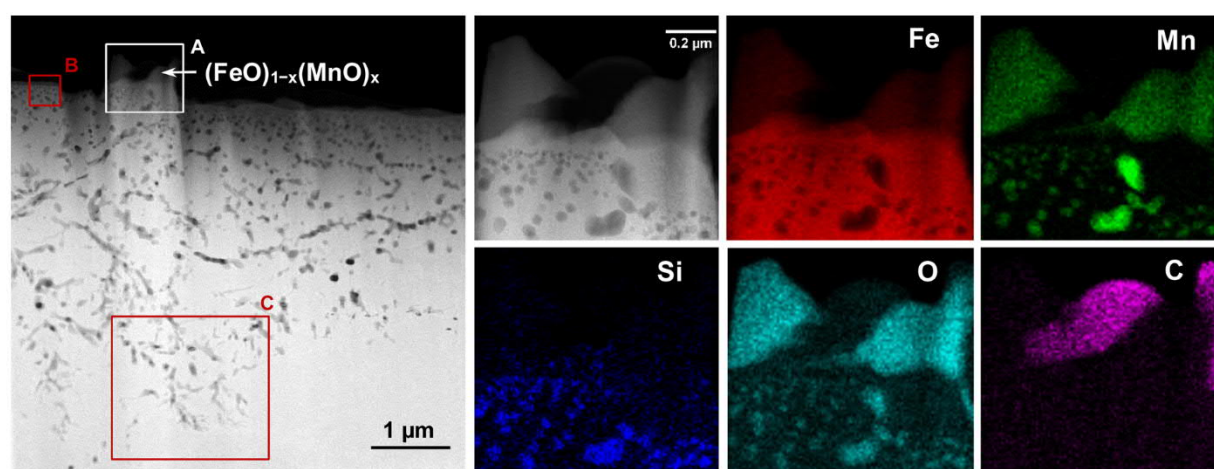

Fig. 7. Cross-sectional HAADF-STEM images of Fe-2 Mn-1 Si after exposure to the 69 vol%H_2 + 31 vol%H_2O gas atmosphere for 2 h at 700 °C and the elemental maps of Fe-Kα, Mn-Kα, Si-Kα, O-Kα and C-Kα from area A.

oxygen-uptake process, i.e., the absorption of O into the metal. Hence, the chemical states of the alloys, post selective oxidation at aforementioned conditions, were characterized using XPS to verify the composition of the oxides close to the surface.

For Fe-2 Mn, the Mn 2p3/2 peak is observed along the entire sputter depth (duration of 2286 s, depth of about 1.1 μm) at binding energies (BEs) from 640.6 to 641.0 eV (Fig. 9a). The minor shift of the Mn 2p3/2 BE peak in $(FeO)_{1-x}(MnO)_x$ regarding 640.5 eV for MnO (Ref. [23]) is probably due to the variation of the overall Fe/Mn ratio which decreases with depth. Besides, a small peak with binding energies ranging from 646.5~646.9 eV can also be detected within the etching duration of 2286 s, which can be ascribed to the shake-up satellite for $(FeO)_{1-x}(MnO)_x$. Fe_2MnO_4 BE peak at 639.8 eV [24] appears before 6 s etching alongside $(FeO)_{1-x}(MnO)_x$, but is absent after 126 s etching.

In the Fe 2p3/2 spectra (Fig. 9b), one Fe 2p3/2 BE peak at 710.7 eV is captured at the outermost surface, assigned to Fe_3O_4 [25] and/or Fe_2MnO_4 [26]. The reason why before sputtering $(FeO)_{1-x}(MnO)_x$ is visible in the Mn 2p3/2 spectrum but not in the Fe 2p3/2 spectrum is most likely because the $(FeO)_{1-x}(MnO)_x$ signals are masked by the very large Fe_3O_4/Fe_2MnO_4 signals in the Fe 2p3/2 spectrum. At 6 s etching, besides the peak at 710.7 eV a small peak at binding energy of ~709.6 eV also appears, which is attributed to $(FeO)_{1-x}(MnO)_x$ (709.6 eV for FeO in Ref. [27]). At 126 s etching, the proportion of $(FeO)_{1-x}(MnO)_x$ significantly increases, and accordingly its shake-up satellite at binding energy of ~715.3 eV becomes obvious. Biesinger et al. [28] also include

a small satellite peak in their fitting for MnO and FeO, with a value of 645.5 eV for the former of Mn 2p3/2 and 715.4 eV for the latter of Fe 2p3/2. At 468 s etching, Fe_3O_4 or Fe_2MnO_4 signals fully disappear, and meanwhile metallic iron with BE peak at 706.7 eV [29] emerges. The Fe/$(FeO)_{1-x}(MnO)_x$ peak-area ratios are steadily increasing until 2286 s of etching. The external Fe_2MnO_4 and Fe_3O_4 oxides are most likely formed during cooling, as can be generated in Fig. 2a.

Throughout the whole sputtered depth of the alloy Fe-2 Mn-0.25 Si (2286 s of etching), the Mn 2p3/2 spectra can be fitted using three components, with the peaks at binding energies of 640.6~641.0 eV and 646.5~646.9 eV assigned to the core level and satellite spectra of $(FeO)_{1-x}(MnO)_x$ respectively and the peak at binding energy of 641.9~642.2 eV assigned to the Mn-Si-mixed oxides (642.0 ± 0.4 eV for Mn_2SiO_4 reported in Ref. [30]) (Fig. 10a). The formation of the Mn-Si-mixed oxides can be further confirmed by identifying the Si 2p spectra.

It is illustrated in Fig. 10b that within the etching duration of 2286 s all the Si 2p spectra are composed of a single BE peak in the range of 101.7–102.5 eV [9]. It is worth noticing that although the amount of Mn-Si-mixed oxides is also considerable, as demonstrated by the considerable peak-area ratios of Mn-Si oxides to $(FeO)_{1-x}(MnO)_x$ in Fig. 10a, Mn-Si oxide phase was not detected by GIXRD. This suggests that Mn-Si oxides are mainly presented in amorphous form, which agrees with the finely dispersed spherical particles in Fig. 8. The minor shift of the BE peak of the Mn-Si oxide is most likely because of the
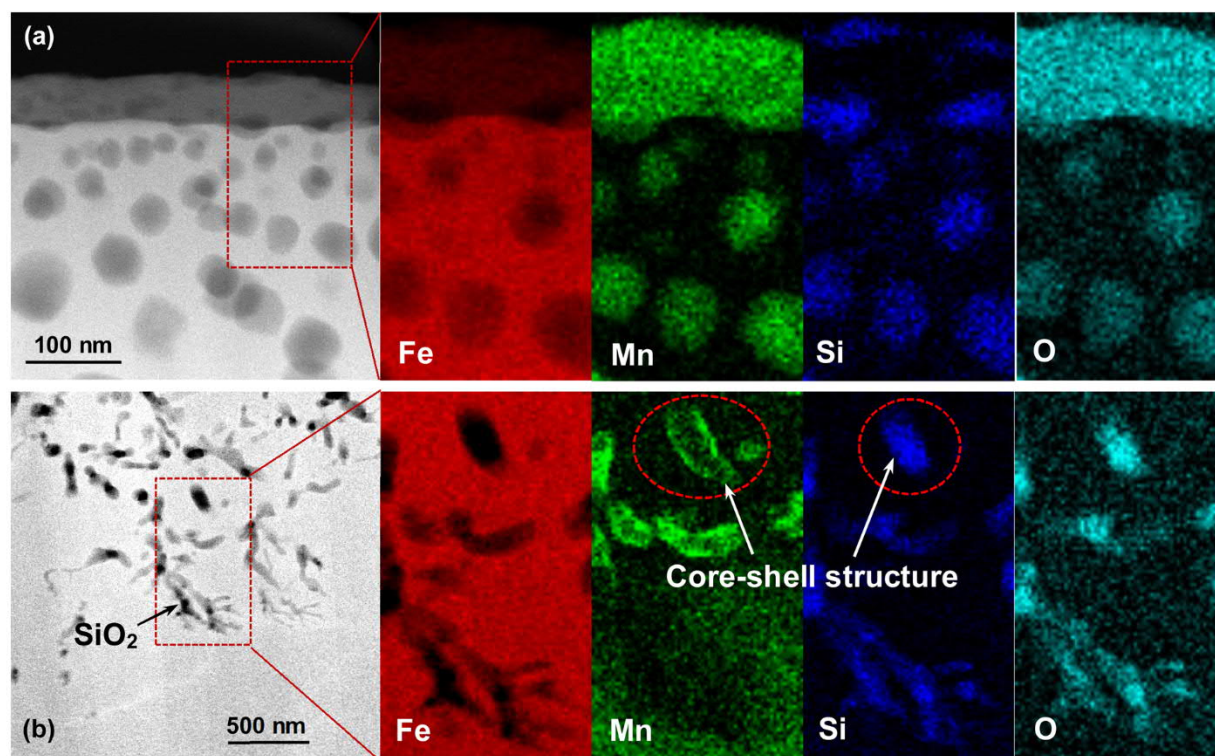
Fig. 8. Cross-sectional HAADF-STEM micrographs of the Fe-2 Mn-1 Si alloy after exposure at 700 °C and $p(O_2) = 2.9 \times 10^{-22}$ bar for 2 h and the corresponding maps of Fe-Kα, Mn-Kα, Si-Kα and O-Kα from areas B (a) and C (b) in Fig. 7.

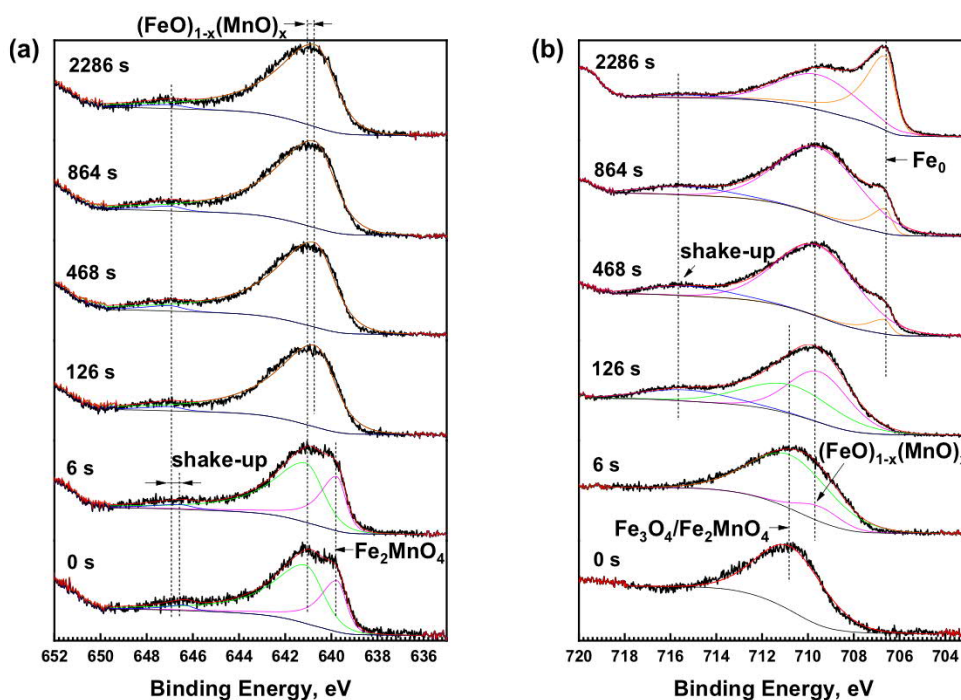**Fig. 9.** XPS spectra of (a) Mn $2p_{3/2}$ and (b) Fe $2p_{3/2}$ for Fe-2 Mn at various depths, after exposure to the 69 vol%H_2 + 31 vol%H_2O gas atmosphere for 2 h at 700 °C.

variation of the manganese-to-silicon ratio and its amorphous nature, with the latter attributed to the change in the neighboring chemical state, as discussed elsewhere [31–33].

The Fe 2p3/2 spectrum obtained at the uppermost surface exhibits a single peak corresponding to Fe_3O_4, as displayed in Fig. 10c. At 6 s etching, the core level spectrum of $(FeO)_{1-x}(MnO)_x$ begins to appear, along with its shake-up peak. At 126 s etching, metallic iron emerges,

whereas Fe_3O_4 vanishes away entirely. The $(FeO)_{1-x}(MnO)_x$ amount at 468 s etching is very low, and further decreases with etching.

Spectra corresponding to Fe-2 Mn-1 Si and Fe-2 Mn-2 Si, shown in Figs. 11 and 12, respectively, are almost identical to those of Fe-2 Mn-0.25 Si. $(FeO)_{1-x}(MnO)_x$ related Fe and Mn XPS signals for Fe-2 Mn-1 Si and Fe-2 Mn-2 Si are correlated to the nodule-like oxides and the film-like oxides at the sample surfaces. The peak area ratios of
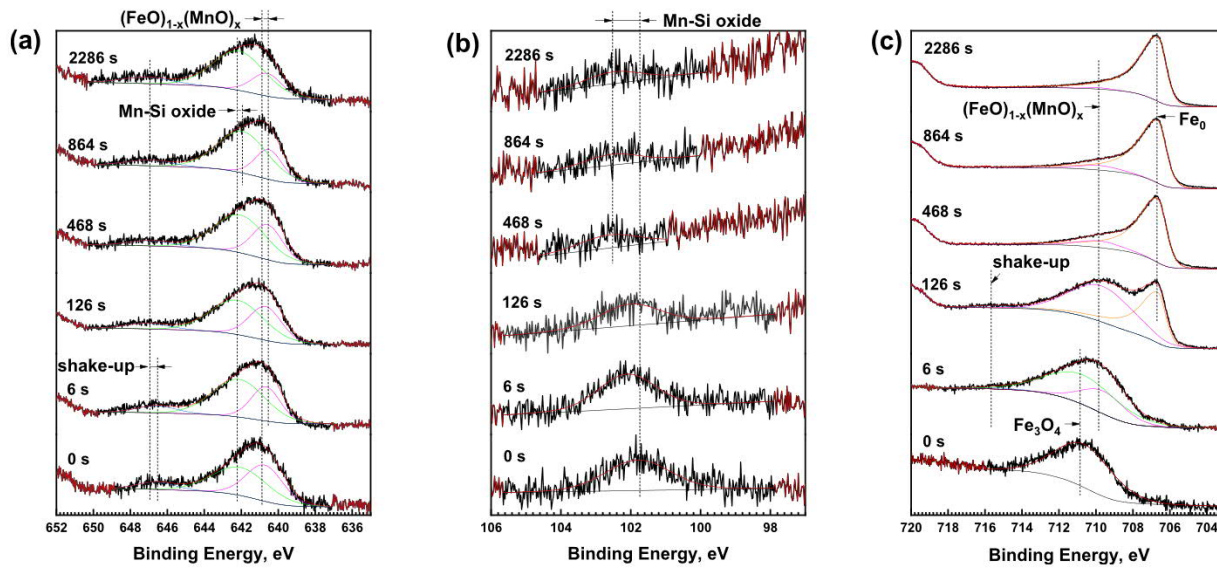
Fig. 10. XPS spectra of (a) Mn $2p_{3/2}$, (b) Si 2p and (c) Fe $2p_{3/2}$ for Fe-2 Mn-0.25 Si at various depths, post exposure at 700 °C and $p(O_2) = 2.9 \times 10^{-22}$ bar for 2 h.
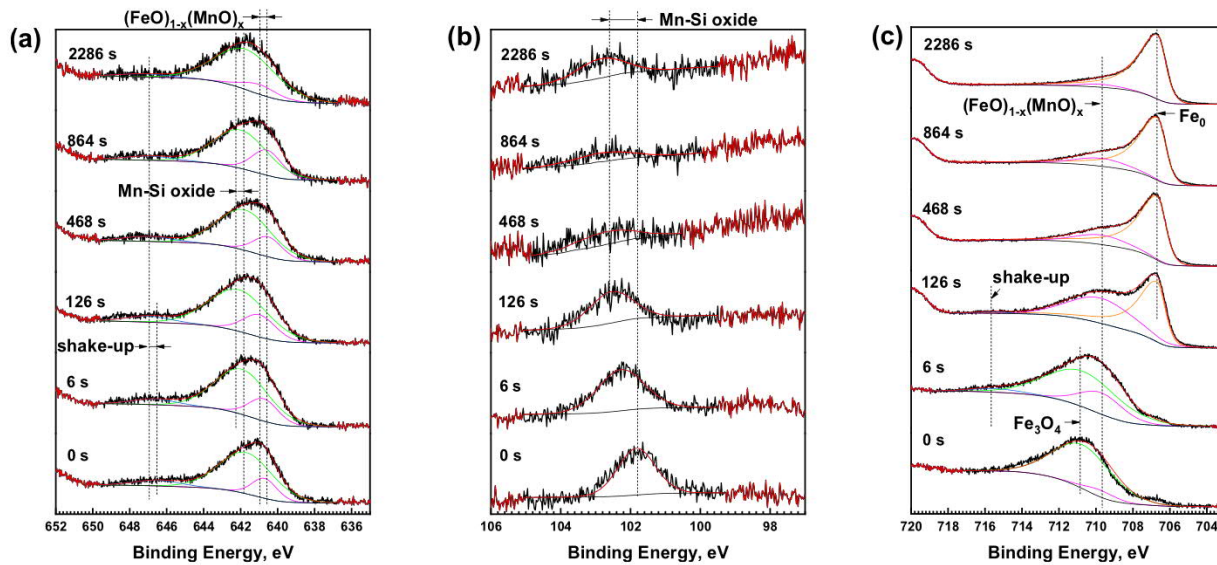

Fig. 11. XPS spectra of (a) Mn $2p_{3/2}$, (b) Si 2p and (c) Fe $2p_{3/2}$ for Fe-2 Mn-1 Si at various depths, post oxidizing at 700 °C and $p(O_2) = 2.9 \times 10^{-22}$ bar for 2 h.

$(FeO)_{1-x}(MnO)_x$ to Fe_0 for Fe-2 Mn-2 Si are larger than its counterparts for Fe-2 Mn-1Si, demonstrating a higher proportion of $(FeO)_{1-x}(MnO)_x$ for the former.

It should be noted that the presence of $(FeO)_{1-x}(MnO)_x$ is not anticipated for Fe-2 Mn-1 Si and Fe-2 Mn-2 Si at aforementioned conditions in this work, as demonstrated in Fig. 2c. However, the increase in Si content results in a higher degree of internal oxidation and a correspondingly larger tensile stress, which is expected to boost the migration of elements to the uppermost surface. The faster outward diffusion rate of manganese [20] in comparison with silicon [21] and iron [22] and hence the corresponding aggregation of manganese at the subsurface facilitate the formation of the outer $(FeO)_{1-x}(MnO)_x$. Similarly, an unexpected MnO was also observed on the surfaces of Fe-2 Mn-1 Si and Fe-2 Mn-2 Si during exposure at a much lower $p(O_2)$ of 6.5×10^{-25} bar [9]. Actually, Fe_2SiO_4 (Fe-Si- or Fe-Mn-Si-mixed oxides in this case) is also thermodynamically expected to form during isothermal exposure at 700 °C in the given gas mixture according to the phase diagram in Fig. 2c. Unfortunately, it is difficult to distinguish Fe_2SiO_4 as its Fe 2p3/2 and Si 2p binding energies [34] resemble those of

$(FeO)_{1-x}(MnO)_x$ and Mn-Si oxides, respectively.

3.4. Discussion

The presented results show that in the prevalent conditions, the oxidation of all the Si-containing alloys follows linear kinetics. This indicates that the rate-determining step at the initial stage which lasts more than 1 or 2 h, is the oxygen uptake. Presence of Si in Fe-Mn based alloys promotes both external and internal oxidation. This is observed more prominently along the grain boundaries. For Fe-2 Mn, a small number of scattered $(FeO)_{1-x}(MnO)_x$ oxides can be observed both on the surface and inside the alloy, with larger particles formed mainly along the grain boundaries. The presence of a thin external $(FeO)_{1-x}(MnO)_x$ layer is attributed to fast bulk diffusion of Mn to the surface. Although the overall oxide growth (mainly internal) of Fe-2 Mn is beyond the resolution limit, it is also suggested to be an uptake-controlled process on account of the similar Fe-2 Mn-based composition and the identical experimental conditions as those for the silicon-containing alloys. In comparison, at lower $p(O_2)$ of 6.5×10^{-25} bar and otherwise same
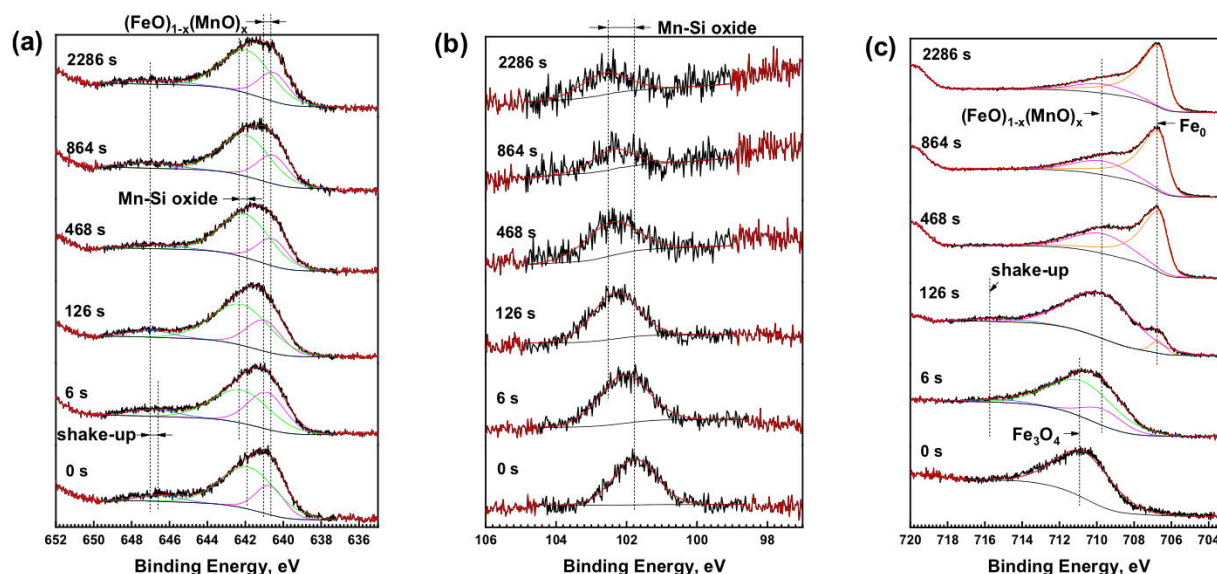
Fig. 12. XPS spectra of (a) Mn 2p$_{3/2}$, (b) Si 2p and (c) Fe 2p$_{3/2}$ for Fe2 Mn-2 Si at various depths, post exposure at 700 °C and $p(O_2) = 2.9 \times 10^{-22}$ bar for 2 h.

conditions [9], the external oxidation was enhanced and internal oxidation was decreased in Fe-2 Mn. The elimination of the external nodule-like oxides at higher oxygen partial pressure is most likely due to an enhanced uptake rate of oxygen and hence a lesser degree of external oxidation. For Fe-2 Mn-0.25 Si, oxides are found predominantly at GBs, along with much finer oxides inside the grains. The presence of the outer ridge-like $(FeO)_{1-x}(MnO)_x$ oxides reveals the pronounced outward migration of manganese and iron along the GBs. The mass increase after 2 h oxidation of Fe-2 Mn-1 Si is almost double of that of Fe-2 Mn-0.25 Si. The depth of the GB oxidation shows only a minor increase whereas the oxide density in the bulk increases significantly. This significant enhancement in the density of the intragranular oxides is probably because the increased alloying content of silicon accelerates the nucleation and the subsequent growth of silicon-containing oxides. Further raising the silicon content to 2 mass% leads to both markedly enhanced intergranular and intragranular oxidation. Besides the facilitated nucleation of silicon-containing oxides a markedly promoted uptake of O has to be concluded as the principal cause for the pronounced internal oxidation of specimens containing higher content of silicon. This is because for all alloys a linear mass gain with time was observed.

At a much lower $p(O_2)$ of 6.5×10^{-25} bar [9], the external oxide layer was determined as MnO for all the Fe-Mn based alloys (with 0–2 mass% silicon). In comparison, external $(FeO)_{1-x}(MnO)_x$ was formed for all the alloys at the much higher oxygen partial pressure of 2.9×10^{-22} bar in this study. The iron/manganese ratio in the $(FeO)_{1-x}(MnO)_x$ oxides decreases with depth, as depicted by the EDX results in Fig. 6, suggesting that the formation of $(FeO)_{1-x}(MnO)_x$ with higher iron content requires a larger oxygen activity. Since the $p(O_2)$ for the manganese/manganese oxide equilibrium is dramatically lower than that of iron/wüstite, manganese oxide is suggested to form first once the local activity of O reaches its thermodynamic commencement. Further increase in the oxygen activity would then lead to the subsequent oxidation also of Fe in contact with MnO and hence incorporation of Fe into the MnO lattice. As the mismatch between Fe and Mn is small in the wüstite structure, inclusion of Fe into MnO may happen at oxygen partial pressures well below the thermodynamic onset of FeO formation. Based on thermodynamic calculation, Mao et al. [35] indeed found that the computed iron concentration in $(FeO)_{1-x}(MnO)_x$ rose with $p(O_2)$ until the dissociation $p(O_2)$ of wüstite.

It is interesting to see that although the reaction kinetics of Fe-2 Mn-x Si exhibit linear behavior in the primary phase (Fig. 1a), the external $(FeO)_{1-x}(MnO)_x$ layer exhibits a surprisingly high thickness, ~60 nm for

Fe-2 Mn-1 Si after 2 h of reaction (Fig. 8a). Noticeably, if transport through the external $(FeO)_{1-x}(MnO)_x$ were rate limiting, then the oxide layer had to reach its final thickness within about 3 min (based on the thermogravimetry data, showing linear growth after 3 min at the latest, see Fig. 1a), as otherwise there would not be linear growth kinetics. However, the external layer formed on Fe-2 Mn-1 Si after 10 min exposure under the same conditions exhibits a much thinner thickness, with an overall value of less than 20 nm (see Figs. A2 and A3). This indicates that the oxygen uptake on the surface or at the oxide scale/matrix interface is the rate-limiting step rather than diffusion through the surface oxide layer. In both cases the transport through the oxide layer has to be even faster than this uptake reaction, as otherwise the latter would not be rate determining.

It is quite impressive that the oxide layer can provide such high rates through the relatively thick $(FeO)_{1-x}(MnO)_x$ layer of about 60 nm. This can be ascribed to the high ionic conductivity of the layer due to the following possible reasons: 1) the $(FeO)_{1-x}(MnO)_x$ phase is intrinsically highly defective at high temperatures due to deficiency in cations [19] (at 700 °C the Fe/O ratio in $Fe_{1-x}O$ varies in a wide range according to the phase diagram [36]), 2) the incorporation of Fe in the MnO crystal introduces more vacancies into the lattice that accelerate the O diffusion, 3) the tensile stress caused by the volume expansion during internal oxidation can further boost the elemental diffusion through the external layer, 4) the number of defects in p-type oxides (($FeO)_{1-x}(MnO)_x$ in this case) increases with increasing oxygen partial pressure [37], 5) based on the semiconductor characteristics, dissolving cations of higher valence into the p-type oxide (i.e. doping Si into $(FeO)_{1-x}(MnO)_x$) facilitates the creation of more cation vacancies and thus enhances the concentration of ionic defects [37]. Consequently, despite the thickness of the oxide layer, mass transport through $(FeO)_{1-x}(MnO)_x$ does not limit the kinetics of oxidation.

On the other hand, the linear mass increase suggests O uptake as the step controlling the reaction rate. The component and content of the outer oxides and the difference in concentration gradient of O at the surface/interface and just beneath the surface/interface are suggested to be the key factors limiting the oxygen-uptake kinetics. The constant uptake rate in the primary oxidation phase of Fe-2 Mn-x Si manifests that the first thin oxide layer must have formed very quickly. Otherwise, the uptake rate would change due to the progressive oxidation of the initially bare surface. It is evident from Figs. A2 and A3 that a continuous thin Fe-Mn oxide layer is already formed on Fe-2 Mn-1 Si after 10 min exposure. The fast formation of the first thin oxide layer is consistent
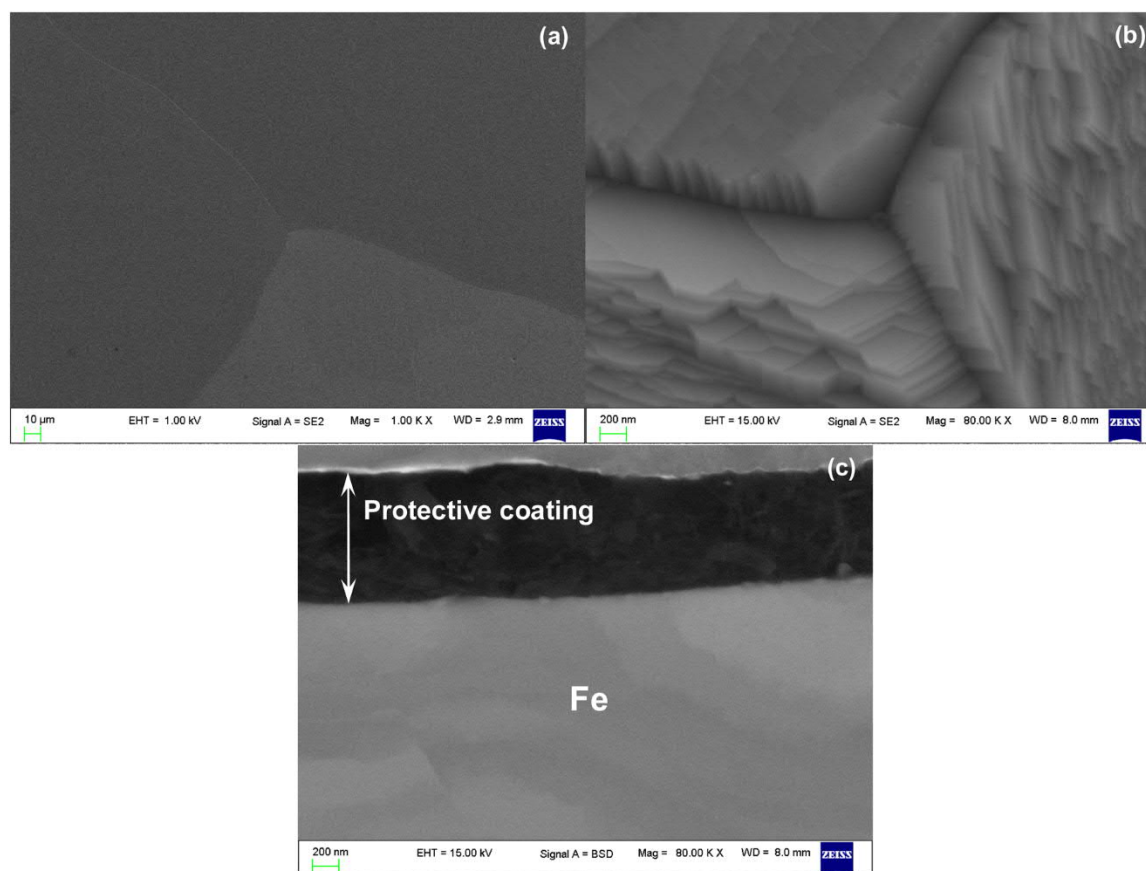
Fig. A1. Surface (a,b) and cross-sectional (c) morphologies of pure Fe after exposure to the 69 vol%H_2 + 31 vol%H_2O gas atmosphere for 2 h at 700 °C. No iron oxides can be observed.

with the observation of an uptake-controlled process of constant rate from the very early stage. Noticeably, the uptake-controlled process might either take place at the oxide surface or at the interface with the alloy. On account of the rather continuous external layers as shown in Figs. 6–8, O uptake at the alloy/scale interface is regarded as the slowest reaction step in the present study.

It is apparent from the aforementioned results that alloys containing higher silicon concentration have a higher demand for uptake of O to support their more severe internal oxidation. As long as the O uptake remains rate-controlling, the diffusion of absorbed oxygen from the interface to the oxidation front can be considered the remarkedly more rapid process. This means that the concentration of oxygen just underneath the interface should be much lower than the thermodynamically required concentration of oxygen for equilibrium at the alloy/scale interface. The oxygen gradient between the oxide scale/alloy interface and the alloy just below it plays a crucial role for the uptake process. This gradient is proposed to be higher for alloys with higher Si contents, considering their enhanced oxygen consumption during internal oxidation and that Si oxidation sets in at much lower oxygen partial pressures than Mn oxidation and that the formed Si oxides also serve as nuclei for the subsequent formation of Mn-containing oxides.

Despite using a $p(O_2)$ almost three orders of magnitude higher than that in our previous report [9], the oxidation kinetics of Fe-2 Mn-1 Si and Fe-2 Mn-2 Si in this study are only 3~4 times faster. This further indicates that the rate-limiting step of internal oxidation is the oxygen-uptake process at the alloy/scale interface. The enhanced oxygen uptake of the respective alloys at higher oxygen partial pressure here can be best attributed to the solid solution of FeO in the MnO layer. Since the oxygen uptake at the alloy/scale interface is rate determining, the highest possible mole fraction of dissolved O at the alloy interface will be the one corresponding to the equilibrium between the scale and

the bulk. Although this equilibrium will not be reached due to fast diffusion, it can give an idea about the effect of the scale: the more FeO in the MnO scale the higher the oxygen activity at the interface will be. Therefore, facilitated O uptake for alloys containing more silicon concentration is correlated to the higher FeO content in the oxide layer on their surface.

4. Conclusions

The oxidation kinetics of iron-manganese-silicon alloys (Fe-2 Mn, Fe-2 Mn-0.25 Si, Fe-2 Mn-1 Si, Fe-2 Mn-2 Si) were analyzed at 700 °C and $p(O_2)$ of 2.9×10^{-22} bar for 2 h. The mass changes of the Fe-2 Mn-x Si alloys were found to follow linear growth kinetics for varying Si contents, indicating the uptake of oxygen as the rate-controlling step for short-term oxidation. The morphology and composition of the external and internal oxides were characterized in depth. An external $(FeO)_{1-x}(MnO)_x$ layer of several tens of nanometers thickness was formed on all the alloys. Nevertheless, the external layer did not impose diffusion inhibition on the oxygen uptake. Silicon addition to Fe-2 Mn was found to enhance internal oxidation, particularly along the grain boundaries for the alloys with lower Si contents. In case of Fe-2 Mn, only small amounts of $(FeO)_{1-x}(MnO)_x$ could be detected inside the alloy. However, for Si-containing alloys, even at a concentration of 0.25 wt.% Si, significant and predominant GB oxidation was formed along with very fine intragranular oxides. Further increase in the Si content led to larger oxidation depths both inside the grains and along the grain boundaries and denser intragranular Si-containing oxides. The observed oxidation depths are much higher than the prediction from Meijering's model when diffusion coefficients from literature are used. This indicates that oxygen diffuses much faster than in alpha iron, most likely due to diffusion along the oxide/matrix phase boundary. The oxides
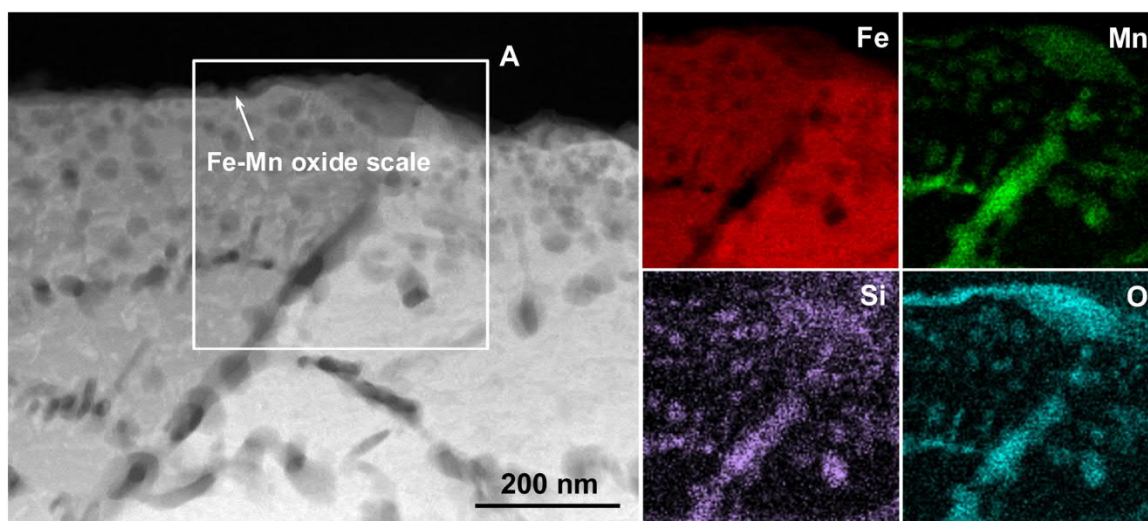
Fig. A2. Cross-sectional HAADF-STEM micrographs of the Fe-2 Mn-1 Si alloy post oxidizing at 700 °C and $p(O_2) = 2.9 \times 10^{-22}$ bar for 10 min and the corresponding maps of Fe-Kα, Mn-Kα, Si-Kα and O-Kα from area A.

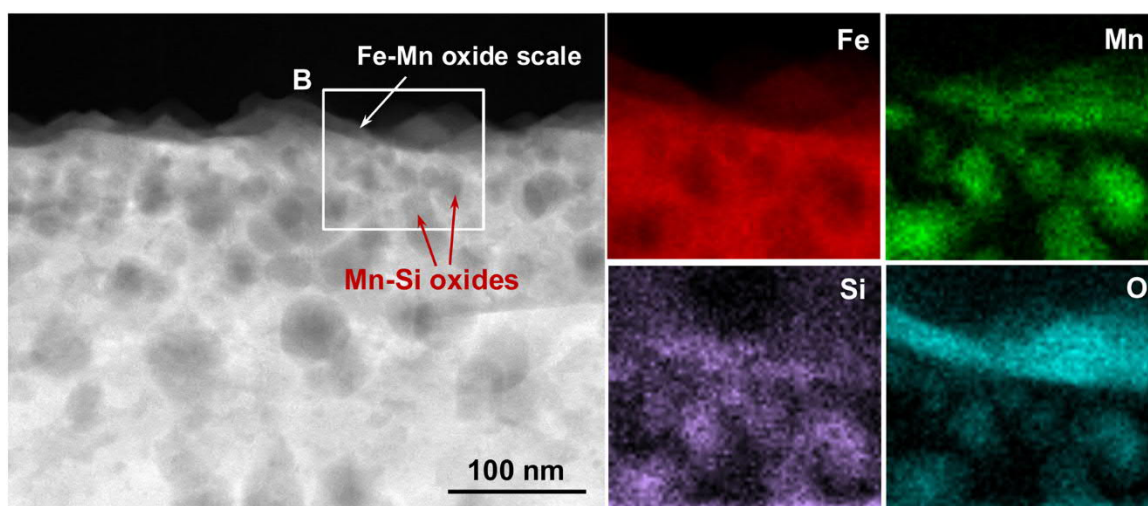**Fig. A3.** Cross-sectional HAADF-STEM micrographs of the Fe-2 Mn-1 Si alloy post oxidizing at 700 °C and $p(O_2) = 2.9 \times 10^{-22}$ bar for 10 min and the elemental maps of Fe-Kα, Mn-Kα, Si-Kα and O-Kα from area B.

close to the oxidation front were mainly composed of SiO_2, slightly above which were mixed oxides with an outer Mn-rich oxide shell embracing a Si-rich oxide core. Besides the easy nucleation of silicon-containing oxides, a significantly enhanced uptake of O is the principal cause for the pronounced internal oxidation of alloys possessing higher silicon content. The surface oxide layer $(FeO)_{1-x}(MnO)_x$ has a crucial influence on the kinetics at the studied annealing conditions. As the FeO content of the oxide layer increases with more silicon concentration in the alloy, the layer is suggested to facilitate the O-uptake kinetics.

Data availability

The raw/processed data required to reproduce these findings cannot be shared at this time due to legal or ethical reasons.

Author statement

Xue Zhang: Conceptualization, Methodology, Investigation, Writing-Original Draft, Writing-Review & Editing. **Cauê Corrêa da Silva**: Investigation & Editing. **Siyuan Zhang**: Investigation & Editing.

Manoj Prabhakar: Investigation & Editing. **Wenjun Lu**: Investigation. **Alexandra Vogel:** Investigation. **Michael Rohwerder**: Validation & Editing.

Declaration of Competing Interest

The authors declare that they have no known competing financial interests or personal relationships that could have appeared to influence the work reported in this paper.

Appendix A

References

[1] G. Frommeyer, U. Brüx, P. Neumann, Supra-ductile and high-strength manganese-TRIP/TWIP steels for high energy absorption purposes, ISIJ Int. 43 (2003) 438–446, https://doi.org/10.2355/isijinternational.43.438.

[2] M. Auinger, V.G. Praig, B. Linder, H. Danninger, Grain boundary oxidation in iron-based alloys, investigated by ^{18}O enriched water vapour - the effect of mixed oxides in binary and ternary Fe-{Al, Cr, Mn, Si} systems, Corros. Sci. 96 (2015) 133–143, https://doi.org/10.1016/j.corsci.2015.04.009.

[3] M. Auinger, E.M. Müller-Lorenz, M. Rohwerder, Modelling and experiment of selective oxidation and nitridation of binary model alloys at 700 °C–The systems Fe, 1 wt.%{Al, Cr, Mn, Si}, Corros. Sci. 90 (2015) 503–510, https://doi.org/10.1016/j.corsci.2014.06.049.

[4] K. Kusabiraki, R. Watanabe, T. Ikehata, M. Takeda, T. Onishi, X.P. Guo, High-temperature oxidation behavior and scale morphology of Si-containing steels, ISIJ Int. 47 (2007) 1329–1334, https://doi.org/10.2355/isijinternational.47.1329.

[5] R.Y. Chen, W.Y.D. Yuen, A study of the scale structure of hot-rolled steel strip by simulated coiling and cooling, Oxid. Met. 53 (2000) 539–560, https://doi.org/10.1023/A:1004637127231.

[6] T. Fukagawa, H. Okada, Y. Maehara, Mechanism of red scale defect formation in Si-added hot-rolled steel sheets, ISIJ Int. 34 (1994) 906–911, https://doi.org/10.2355/isijinternational.34.906.

[7] R.Y. Chen, W.Y.D. Yuen, Oxide-scale structures formed on commercial hot-rolled steel strip and their formation mechanisms, Oxid. Met. 56 (2001) 89–118, https://doi.org/10.1023/A:1010395419981.

[8] T. Kizu, Y. Nagataki, T. Inazumi, Y. Hosoya, Intergranular and internal oxidation during hot-rolling process in ultra-low carbon steel, ISIJ Int. 42 (2002) 206–214, https://doi.org/10.2355/isijinternational.42.206.

[9] X. Zhang, C. Corrêa da Silva, C. Liu, M. Prabhakar, M. Rohwerder, Selective oxidation of ternary Fe-Mn-Si alloys during annealing process, Corros. Sci. 174 (2020) 108859, https://doi.org/10.1016/j.corsci.2020.108859.

[10] H.C. Liu, F. Li, W. Shi, S. Swaminathan, Y.L. He, M. Rohwerder, L. Li, Challenges in hot-dip galvanizing of high strength dual phase steel: surface selective oxidation and mechanical property degradation, Surf. Coat. Tech. 206 (2012) 3428–3436, https://doi.org/10.1016/j.surfcoat.2012.02.001.

[11] S. Frenznick, S. Swaminathan, M. Stratmann, M. Rohwerder, A novel approach to determine high temperature wettability and interfacial reactions in liquid metal/solid interface, J. Mater. Sci. 45 (2010) 2106–2111, https://doi.org/10.1007/s10853-009-4147-7.

[12] M. Auinger, A. Vogel, D. Vogel, M. Rohwerder, Early stages of oxidation observed by in situ thermogravimetry in low pressure atmospheres, Corros. Sci. 86 (2014) 183–188, https://doi.org/10.1016/j.corsci.2014.05.010.

[13] S.Y. Zhang, I. Ahmet, S.H. Kim, O. Kasian, Different photostability of BiVO$_4$ in near-pH-neutral electrolytes, ACSAEM 3 (2020) 9523–9527, https://doi.org/10.1021/acsaem.0c01904.

[14] S.Y. Zhang, C. Scheu, Evaluation of EELS spectrum imaging data by spectral components and factors from multivariate analysis, Microscopy 67 (2018) i133–i141, https://doi.org/10.1093/jmicro/dfx091.

[15] A.H. Jay, K.W. Andrews, Note on oxide systems pertaining to steel - making furnace slags: FeO-MnO, FeO-MgO, CaO-MnO, MgO-MnO, J. Iron Steel Inst. 152 (1946) 15–18.

[16] J.A.A. Leroux, E. Raub, Untersuchungen über das Verhalten von Silber und Silber-Kupferlegierungen beim Glühen in Sauerstoff und Luft, Z. Anorg. Allg. Chem. 188 (1930) 205–231, https://doi.org/10.1002/zaac.19301880119.

[17] H.C. Yi, S.W. Guan, W.W. Smeltzer, A. Petric, Internal oxidation of Ni-Al and Ni-Al-Si alloys at the dissociation pressure of NiO, Acta Met. Mat. 42 (1994) 981–990, https://doi.org/10.1016/0956-7151(94)90292-5.

[18] G. Schimmel, J. Sorina-Muller, B. Kempf, M. Rettenmayr, On the mechanism of Ag exudation during internal oxidation, Acta Mater. 58 (2010) 2091–2102, https://doi.org/10.1016/j.actamat.2009.11.051.

[19] D.J. Young, High Temperature Oxidation and Corrosion of Metals, 2nd edition, Elsevier, 2016.

[20] K. Nohara, K.I. Hirano, Diffusion of Mn54 in iron and iron-manganese alloys, Proc. ICSTIS, Suppl. Trans. ISIJ 11 (1971) 1267–1273.

[21] W. Batz, H.W. Mead, C.E. Birchenall, Diffusion of silicon in iron, J. Met. 4 (1952), https://doi.org/10.1007/BF03397772, 1070-1070.

[22] H. Mehrer, L. Börnstein, Numerical Data and Functional Relationships in Science and Technology: Group III, Springer, Berlin, 1990.

[23] M. Oku, K. Hirokawa, X-ray photoelectron spectroscopy of Co3O4, Fe3O4, Mn3O4, and related compounds, J. Electron Spectrosc. Relat. Phenom. 8 (1976) 475–481, https://doi.org/10.1016/0368-2048(76)80034-5.

[24] V.A.M. Brabers, F.M. Van Setten, P.S.A. Knapen, X-ray photoelectron spectroscopy study of the cation valencies in nickel manganite, J. Solid State Chem. 49 (1983) 93–98, https://doi.org/10.1016/0022-4596(83)90220-7.

[25] P. Mills, J.L. Sullivan, A study of the core level electrons in iron and its three oxides by means of X-ray photoelectron spectroscopy, J. Phys. D Appl. Phys. 16 (1983) 723–732, https://doi.org/10.1088/0022-3727/16/5/005.

[26] G.C. Allen, S.J. Harris, J.A. Jutson, A study of a number of mixed transition metal oxide spinels using X-ray photoelectron spectroscopy, Appl. Surf. Sci. 37 (1989) 111–134, https://doi.org/10.1016/0169-4332(89)90977-X.

[27] P. Mills, J.L. Sullivan, A study of the core level electrons in iron and its three oxides by means of X-ray photoelectron spectroscopy, J. Phys. D 16 (1983) 723–732, https://doi.org/10.1088/0022-3727/16/5/005.

[28] M.C. Biesinger, B.P. Payne, A.P. Grosvenor, L.W.M. Lau, A.R. Gerson, R.St.C. Smart, Resolving surface chemical states in XPS analysis of first row transition metals, oxides and hydroxides: Cr, Mn, Fe, Co and Ni, Appl. Surf. Sci. 257 (2011) 2717–2730, https://doi.org/10.1016/j.apsusc.2010.10.051.

[29] C.E. Myers, H.F. Franzen, J.W. Anderegg, X-ray photoelectron spectra and bonding in transition metal phosphides, Inorg. Chem. 24 (1985) 1822–1824, https://doi.org/10.1021/ic00206a025.

[30] A. Ollivier-Leduc, M.L. Giorgi, D. Balloy, J.B. Guillot, Nucleation and growth of selective oxide particles on ferritic steel, Corros. Sci. 52 (2010) 2498–2504, https://doi.org/10.1016/j.corsci.2010.03.030.

[31] A. Mekki, D. Holland, C.F. McConville, M. Salim, An XPS study of iron sodium silicate glass surfaces, J. Non-Cryst. Solids 208 (1996) 267–276, https://doi.org/10.1016/S0022-3093(96)00523-6.

[32] T.C. Taucher, I. Hehn, O.T. Hofmann, M. Zharnikov, E. Zojer, Understanding chemical versus electrostatic shifts in X-ray photoelectron spectra of organic self-assembled monolayers, J. Phys. Chem. C 120 (2016) 3428–3437, https://doi.org/10.1021/acs.jpcc.5b12387.

[33] B.W. Veal, D.J. Lam, A.P. Paulikas, XPS study of CaO in sodium silicate glass, J. Non-Cryst. Solids 49 (1982) 309–320, https://doi.org/10.1016/0022-3093(82)90127-2.

[34] T. Yamashita, P. Hayes, Analysis of XPS spectra of Fe^{2+} and Fe^{3+} ions in oxide materials, Appl. Surf. Sci. 254 (2008) 2441–2449, https://doi.org/10.1016/j.apsusc.2007.09.063.

[35] W.C. Mao, W.G. Sloof, Relation between oxygen activity gradient in the internal oxidation zone of Mn alloyed steel and the composition of oxide precipitates, Scr. Mater. 135 (2017) 29–32, https://doi.org/10.1016/j.scriptamat.2017.03.009.

[36] Y.W. Fei, S.K. Saxena, A thermochemical data base for phase equilibria in the system Fe-Mg-Si-O at high pressure and temperature, Phys. Chem. Miner. 13 (1986) 311–324, https://doi.org/10.1007/BF00308348.

[37] N. Birks, G.H. Meier, F.S. Pettit, Introduction to the High Temperature Oxidation of Metals, 2nd edition, 2006. Cambridge, UK.